



## Article

# One-Pot Thermal Synthesis of g-C<sub>3</sub>N<sub>4</sub>/ZnO Composites for the Degradation of 5-Fluorouracil Cytostatic Drug under UV-LED Irradiation

Álvaro Pérez-Molina , Luisa M. Pastrana-Martínez , Lorena T. Pérez-Poyatos , Sergio Morales-Torres \* and Francisco J. Maldonado-Hódar

NanoTech—Nanomaterials and Sustainable Chemical Technologies, Department of Inorganic Chemistry, Faculty of Sciences, University of Granada, Avda. Fuente Nueva, s/n, ES-18071 Granada, Spain; alpemo@ugr.es (Á.P.-M.); lpastrana@ugr.es (L.M.P.-M.); lorenaperez@correo.ugr.es (L.T.P.-P.); fjmaldon@ugr.es (F.J.M.-H.)

\* Correspondence: semoto@ugr.es; Tel.: +34-958-248-489

**Abstract:** Graphitic carbon nitride (g-C<sub>3</sub>N<sub>4</sub>) was used to enhance the photocatalytic activity of ZnO nanoparticles for the degradation of 5-fluorouracil (5-FU) cytostatic drug under UV-LED irradiation. CN/ZnO composites were synthesized by an easy one-pot thermal method, varying the g-C<sub>3</sub>N<sub>4</sub> loading, i.e., from 10 to 67 wt% and a post-thermal exfoliation in air. The physicochemical and optical properties of the materials were analyzed by several techniques. CN/ZnO composites showed a coral-like structure of spherical ZnO wurtzite particles on the g-C<sub>3</sub>N<sub>4</sub> structure. In general, the synergism and heterojunction interface between both phases allowed the enhancement of the mesoporosity, light absorption ability, and the aromaticity of the corresponding composites. Moreover, the photocatalytic activity of the CN/ZnO composites was increased with the addition of g-C<sub>3</sub>N<sub>4</sub> in comparison with pristine ZnO. The highest activity was found for the composite containing 25 wt% of g-C<sub>3</sub>N<sub>4</sub> (i.e., CN25/ZnO), reaching the total degradation of 5-FU and a mineralization of 48% at 180 min, as well as a good photostability during four reuse cycles. Experiments with different pH solutions and scavengers allowed for the assessment of the reactive oxygen species (ROS) involved in the 5-FU degradation pathway, with radicals and non-radical species as the main responsible active species. Furthermore, a tentative photocatalytic mechanism was proposed for CN/ZnO composites.

**Keywords:** carbon nitride; zinc oxide; photocatalysis; 5-fluorouracil; water treatment; scavengers



**Citation:** Pérez-Molina, Á.; Pastrana-Martínez, L.M.; Pérez-Poyatos, L.T.; Morales-Torres, S.; Maldonado-Hódar, F.J. One-Pot Thermal Synthesis of g-C<sub>3</sub>N<sub>4</sub>/ZnO Composites for the Degradation of 5-Fluorouracil Cytostatic Drug under UV-LED Irradiation. *Nanomaterials* **2022**, *12*, 340. <https://doi.org/10.3390/nano12030340>

Academic Editors:  
Evgeny Gerasimov and  
Zoltan Konya

Received: 17 November 2021

Accepted: 18 January 2022

Published: 21 January 2022

**Publisher's Note:** MDPI stays neutral with regard to jurisdictional claims in published maps and institutional affiliations.



**Copyright:** © 2022 by the authors. Licensee MDPI, Basel, Switzerland. This article is an open access article distributed under the terms and conditions of the Creative Commons Attribution (CC BY) license (<https://creativecommons.org/licenses/by/4.0/>).

## 1. Introduction

An intensive agriculture and livestock activity, as well as increased industrial discharges and a growing population play a prominent role in the decrease of natural water resources quality. This leads to a marked impact in the middle or long-term effect on the environment, wild life, and human health. During the last decades, a vast number of pollutants has been detected in effluents from municipal wastewater treatment plants (WWTPs), river water, seawater, groundwater and even, tap water [1]. Contaminants of emerging concern (CECs) include a wide family of compounds, such as dyes, pesticides, pharmaceuticals, food additives, personal care products, industrial compounds, hormones, endocrine disruptors, and so on. [2]. Cytostatic drugs, also known as cytotoxic, antineoplastic or anticancer drugs, are a group of pharmaceuticals extensively used to prevent the growth or to inhibit cancer cell activity. In general, pharmaceuticals are not completely metabolized by the patients, part of them are excreted through the urine and/or feces. Furthermore, these pollutants cannot be removed efficiently in conventional WWTPs and as a consequence, are discharged and accumulated into seas and oceans. The 5-Fluorouracil (5-FU) is the active substance of capecitabine pharmaceutical and is classified as an antimetabolite due to its inhibitory mechanism of nuclear RNA exosome complex and tumor growth [3,4]. The

physicochemical properties of 5-FU are relevant for the determination of its environmental action and the effects on human health and wild life. In fact, this pharmaceutical can be persistent in water resources as a consequence of its high mobility in sediment and/or soil ( $K_{oc}$  8), low adsorption into suspended solids, and small octanol–water partition coefficient ( $K_{ow}$   $10^{-0.89}$ ) [5]. Therefore, 5-FU is one of the most commonly used drugs in cancer therapy and has been detected in hospital wastewater at low concentrations ( $\mu\text{g L}^{-1}$ ) and natural waters ( $\text{ng L}^{-1}$ ) from most of European, North, and South American countries, as well as Japan and China [6,7].

Advanced oxidation processes (AOPs) have proven their effectiveness for the removal of pollutants in water through the generation of highly reactive radicals (e.g., hydroxyl radicals,  $\bullet\text{OH}$ ). Among AOPs, heterogeneous photocatalysis is an attractive option since it can be applied using sunlight and non-toxic materials, resulting in a carbon footprint reduction. In the last years, graphitic carbon nitride (g- $\text{C}_3\text{N}_4$ ) has emerged as an interesting photocatalyst due to its effective light harvesting, accompanied by a narrow band gap (i.e., 2.7 eV) and high photocatalytic activity for the degradation of different organic pollutants in aqueous solution [8]. This polymeric semiconductor presents strong carbon–nitrogen covalent bonds providing a high chemical and thermal stability and high electronic conductivity due to a delocalized conjugated structure [9]. Nevertheless, its practical application is still limited by the low light absorption coefficient, poor porosity, and low-charge carrier mobility. Different strategies have been investigated to improve the chemical and texture properties, as well as the charge separation of g- $\text{C}_3\text{N}_4$ , namely, using different precursors [10], synthesis, and post-treatment techniques [11,12], doping with metals and non-metals [13,14], in combination with carbon materials [15–18] and semiconductor heterojunction [19,20], among others.

An effective approach for promoting the charge transfer and retarding the electron-hole recombination rate is the development of composites using two different semiconductors with appropriate valence and conduction band potentials. Zinc oxide (ZnO) is a widely investigated photocatalyst with comparable properties to  $\text{TiO}_2$ , such as non-toxic nature, high activity under UV radiation, low cost [21,22], and rapid recombination of photogenerated electron–hole pairs [23,24]. Furthermore, ZnO can be hybridized with g- $\text{C}_3\text{N}_4$  resulting in g- $\text{C}_3\text{N}_4$ /ZnO composites with an enhanced visible radiation absorption and charge separation in the electron transfer process [8,9,25]. Several methods have been studied to synthesize g- $\text{C}_3\text{N}_4$ /ZnO composites for different photocatalytic applications, namely photoreduction of  $\text{CO}_2$ , production of  $\text{H}_2$  by water spitting, degradation of organic pollutants, etc. Zhu et al. [26] reported the synthesis of carbon-doped g- $\text{C}_3\text{N}_4$ /ZnO composites by the one-step calcination method using dicyandiamide as precursor of g- $\text{C}_3\text{N}_4$  and a carbon source to replace the lattice oxygen of the ZnO structure. The best catalytic performance was obtained with a catalyst containing a ~50 wt% of g- $\text{C}_3\text{N}_4$  for the degradation of methylene blue (MB) under visible radiation ( $\lambda > 400$  nm). The same g- $\text{C}_3\text{N}_4$  content was also found in the g- $\text{C}_3\text{N}_4$ /ZnO composites for the degradation of methyl orange [27] and amiloride [28] under visible light irradiation. Nevertheless, other authors have reported the best catalytic performance for g- $\text{C}_3\text{N}_4$ /ZnO composites containing a lower g- $\text{C}_3\text{N}_4$  content [29–32]. Therefore, Liu et al. [29] concluded that 5.0 wt% of g- $\text{C}_3\text{N}_4$  in g- $\text{C}_3\text{N}_4$ /ZnO composites led to the highest activity for the photooxidation of rhodamine B (RhB) and the photoreduction of  $\text{Cr}^{6+}$  under visible light irradiation, while 10 wt% of g- $\text{C}_3\text{N}_4$  was determined to be the optimum amount for the removal of RhB over g- $\text{C}_3\text{N}_4$  coated hollow pencil-like ZnO composites [32]. Recently, Naseri et al. [31] prepared g- $\text{C}_3\text{N}_4$ /ZnO nanofibers via an electrospinning technique for the degradation of MB under simulated solar radiation. The best catalytic performance was achieved with a composite containing 0.25 wt% of g- $\text{C}_3\text{N}_4$ .

Overall, the photocatalytic performance of g- $\text{C}_3\text{N}_4$ /ZnO composites is not only affected by different synthesis conditions, such as the  $\text{C}_3\text{N}_4$  precursor, the employed method, the g- $\text{C}_3\text{N}_4$ /ZnO ratio, but also the type of pollutant and the irradiation source studied. In the present work, the one-pot thermal decomposition route was studied for the synthesis

of g-C<sub>3</sub>N<sub>4</sub>/ZnO composites using melamine and zinc nitrate, as precursors of g-C<sub>3</sub>N<sub>4</sub> and ZnO, respectively. The optimum g-C<sub>3</sub>N<sub>4</sub>/ZnO ratio was studied for the photodegradation of the 5-FU cytostatic drug under UV-LED irradiation. The 5-FU contaminant has not been previously studied with g-C<sub>3</sub>N<sub>4</sub> materials, while UV-LED systems were demonstrated as energetically efficient, compact, do not heat the solution and with longer half-life and higher quantum yield than the conventional illumination systems based on UV-Vis lamps. The physicochemical, crystallographic and optical properties of the composites were studied by several techniques with a special emphasis on the investigation of possible correlations and synergistic effects between the properties and composition of the composites. Additional photocatalytic experiments using different scavengers and consecutive reaction cycles were carried out to assess the possible reaction mechanism and the photocatalyst stability, respectively.

## 2. Materials and Methods

### 2.1. Synthesis of g-C<sub>3</sub>N<sub>4</sub>/ZnO Composites

Graphitic-C<sub>3</sub>N<sub>4</sub>/ZnO composites (hereafter CN/ZnO) were prepared by an easy thermal treatment for the simultaneous decomposition of melamine (C<sub>3</sub>H<sub>2</sub>N<sub>6</sub>, 99%, VWR Chemicals, Leuven, Belgium) and zinc nitrate tetrahydrate (Zn(NO<sub>3</sub>)<sub>2</sub> · 4H<sub>2</sub>O, 98.5%, Merck, Darmstadt, Germany) following a methodology adapted from [11]. Melamine was selected as the g-C<sub>3</sub>N<sub>4</sub> precursor taking into account preliminary results (not shown) and as cheaper than other typical precursors reported in the literature, such as urea, thiourea, cyanamide, etc. In a typical procedure, a certain amount of melamine and Zn(NO<sub>3</sub>)<sub>2</sub> was mechanically mixed for 10 min and the resulting mixture was placed in a semi-closed crucible inside a muffle furnace (Carbolite, ELF 11/148 model, Hope Valley, UK) under static air atmosphere at 2 °C min<sup>-1</sup> up to 450 °C for 2 h. Then, the temperature was increased up to 550 °C for 4 h under the same experimental conditions. Finally, the synthesized materials were washed repeatedly with distilled water in order to remove the unreacted precursors, and then dried at 60 °C overnight.

Subsequently, a thermal post-treatment over the composites was carried out with some portions of the samples in a semi-open crucible placed into a muffle furnace at 500 °C for 2 h under static air atmosphere, with the aim of increasing the surface area and the charge separation efficiency of the resulting composites [11]. The mass ratio of melamine/Zn(NO<sub>3</sub>)<sub>2</sub> was changed in order to obtain CN/ZnO composites with 10, 25, 50, and 67 wt% of g-C<sub>3</sub>N<sub>4</sub>, the samples were referred as CN10/ZnO, CN25/ZnO, CN50/ZnO, and CN67/ZnO, respectively. For comparison purposes, pure g-C<sub>3</sub>N<sub>4</sub> (sample CN) and pristine ZnO were also synthesized following the same methodology, but without any amount of Zn(NO<sub>3</sub>)<sub>2</sub> and melamine, respectively.

### 2.2. Characterization Techniques

The X-ray diffraction (XRD) patterns were recorded by a Philips PW 1710 diffractometer (Bruker, Rivas-Vacia, Madrid, Spain) using the CuK $\alpha$  radiation and a nickel filter that removes the  $\kappa\beta$  radiation. The crystallite size ( $d_{\text{ZnO}}$ ) of the materials was calculated by applying the Scherrer equation to the highest diffraction peak, which was corresponding to the (101) lattice plane of the hexagonal wurtzite structure (JCPDS card no. 36-1451). Fourier-transform infrared spectra (FTIR) were recorded in a NICOLET 510P spectrometer (Thermo Fisher Scientific, Waltham, MA, USA) with an attenuated total reflection (ATR) accessory and a ZnSn as ATR crystal. The N<sub>2</sub> adsorption–desorption isotherms at –196 °C were carried out using the Quadrasorb SI equipment (Quantachrome, Boston Beach, FL, USA). Previously, the samples were outgassed under high vacuum (10<sup>-6</sup> mbar) at 110 °C for 12 h. The Brunauer–Emmett–Teller (BET) equation was applied to calculate the apparent surface area ( $S_{\text{BET}}$ ) [33,34]. Total pore volume ( $V_{\text{total}}$ ) and mesopore volume ( $V_{\text{meso}}$ ) were determined by applying the Barret–Joyner–Halenda (BJH) method [35] to the desorption branch. The morphology of the prepared materials was studied by scanning electron microscopy (SEM) using a LEO (Carl Zeiss) GEMINI-1430VP microscope (Oberkochen,

Germany). X-ray photoelectron spectroscopy (XPS) was carried out using a Physical Electronics VersaProbe II apparatus (PHI, Chanhassen, MN, USA) equipped with a MgK $\alpha$  X-ray source ( $h\nu = 1486.6$  eV) working at 1.3 V and 20 mA, and a hemispherical electron analyzer. Survey and multi-region spectra were recorded at the C1s, N1s, O1s, and Zn2p photoelectron peaks. The optical properties of photocatalysts were studied by the UV-Vis spectrophotometer CARY 5E (VARIAN, Palo Alto, CA, USA) equipped with a diffuse reflectance accessory (DRA). The spectra in diffuse reflectance mode were transformed to equivalent Kubelka–Munk units. The band gap of the photocatalysts was determined from the corresponding Tauc's plots using Kubelka–Munk units  $(K-M\cdot E)^{1/2}$  as a function of energy (eV) [36]. The point zero of charge ( $pH_{PZC}$ ) of the materials was determined following a pH drift test, as described in [37,38]. Briefly, nitrogen was first bubbled in distillate water with the aim of the prevention of carbon dioxide dissolution and respective water acidification. Then, solutions with varying initial pH (2–12) were prepared using HCl ( $0.1 \text{ mol L}^{-1}$ ) or NaOH ( $0.1 \text{ mol L}^{-1}$ ) and 50 mL of NaCl ( $0.01 \text{ mol L}^{-1}$ ) as electrolyte. Each solution was contacted with 0.10 g of the material and the final pH was measured after 24 h of continuous stirring at room temperature. The PZC value of the material was determined by intercepting the obtained final-pH vs. initial-pH curve with the straight line final-pH = initial-pH.

### 2.3. Photocatalytic Experiments

The photocatalytic performance of the materials was studied for the degradation of 5-FU ( $C_4H_3FN_2O_2$ , >99%, Tokyo Chemical Industry, Tokyo, Japan) in aqueous solution under UV-LED irradiation and at room temperature. The photocatalytic tests were carried out in a refrigerated glass reactor loaded with 100 mL of aqueous solution containing the 5-FU cytostatic drug (154 mM). The photocatalyst load was fixed as  $1 \text{ g L}^{-1}$  and the suspension was continuously stirred with a magnet and with an oxygen flow as purge. The oxygen was allowed to saturate the photocatalyst suspension in order to obtain a high dissolved oxygen concentration in the reaction media, since it has an influence on the photocatalytic activity [39]. The irradiation was performed using a 10 W high-intensity UV-LED ( $15.5 \times 23$  mm) with a maximum irradiance wavelength at 385 nm. In order to achieve the adsorption–desorption equilibrium, the suspension was maintained in a dark period for 30 min before turning on the LED. The reaction in the absence of photocatalysts (photolysis) was also carried out under similar experimental conditions. Moreover, an additional experiment with nitrogen purge rather than oxygen continuous flow was performed for comparison purposes.

During the adsorption and reaction stages, small aliquots were periodically withdrawn from the reactor at different time intervals and the photocatalyst was separated with a  $0.45 \mu\text{m}$  polyethersulfone (PES) filter (Agilent Technologies, Santa Clara, CA, USA). In all of the photocatalytic experiments, the concentration of 5-FU ( $\lambda_{\text{max}} = 265$  nm) was monitored by ultra-high performance liquid chromatography (UHPLC), using the Shimadzu Corporation apparatus (Nexera model, Tokyo, Japan) equipped with a pump LC-30AD, an autosampler SIL-30AC, an oven CTO-20AC, a degasser DGU-20A5r, a system controller CBM-20 A Lite, and a diode array detector (SPD-M20A). Chromatographic separation was carried out using a Shim-pack GISS-HP C18,  $3 \mu\text{m}$  column ( $100 \times 3.0$  mm ID) provided by Shimadzu Corporation (Tokyo, Japan). The injection volume was  $20 \mu\text{L}$ , while the temperature of the column oven and autosampler was set at 30 and  $15^\circ\text{C}$ , respectively. The mobile phase consisted of a mixture of water and methanol (97:3 *v/v*) at isocratic mode and a flow rate of  $0.2 \text{ mL min}^{-1}$ .

The photocatalytic degradation was calculated using the following equation:

$$[5 - \text{FU}] = [5 - \text{FU}]_0 \times e^{-k'_{ap} \times t} \quad (1)$$

where  $[5\text{-FU}]_0$  and  $[5\text{-FU}]$  denote the pollutant concentration at  $t = 0$  and  $t = t$ , respectively,  $k'_{ap}$  is the pseudo-first order kinetic constant, and  $t$  is the reaction time. The values of  $k'_{ap}$  were calculated by non-linear regression.

Total organic carbon (TOC) analysis was performed in the Shimadzu TOC-5000A apparatus (Tokyo, Japan). The TOC content of initial and final samples was studied for selected reactions. Additional photocatalytic experiments were performed to determine the optimum pH solution and photocatalyst stability. The photodegradation of 5-FU was assessed at different pH values, i.e., 3.0, 6.3 (natural), and 9.0, by adding HCl 0.1 M or NaOH 0.1 M, respectively. The photocatalytic degradation pathway of 5-FU was evaluated using methanol (MeOH, 1.0 mM), furfuryl alcohol (FFA, 1.0 mM), and ethylenediaminetetraacetic acid (EDTA, 1.0 mM), as radical, singlet oxygen ( $^1\text{O}_2$ ), and hole scavengers, respectively [40,41].

### 3. Results

#### 3.1. Material Characterization

The occurrence of both  $g\text{-C}_3\text{N}_4$  and ZnO phases in CN/ZnO composites was studied by ATR-IR. Figure 1a shows the corresponding spectra for pure CN, pristine ZnO, and their composites. Pure CN showed several peaks between  $1200\text{--}1650\text{ cm}^{-1}$  associated with the typical stretching vibration of  $g\text{-C}_3\text{N}_4$  heterocycles. The bands placed at  $806$  and  $1417\text{ cm}^{-1}$  were assigned to the s-triazazine ring modes, while the peaks at around  $1330$  and  $1645\text{ cm}^{-1}$  are attributed to C–N and C=N bonds, respectively. The broad band between  $3000\text{--}3500\text{ cm}^{-1}$  belongs to deformation and stretching modes of N–H bonds [42–44]. As expected, the spectra of ZnO presented a high intensity peak at  $\sim 500\text{--}550\text{ cm}^{-1}$  due to the stretching vibration of Zn–O bonds [22]. The spectra of CN/ZnO composites show only the band characteristics of CN at high CN content (67 wt%). However, when the presence of Zn–O bonds increases beyond 50 wt%, the predominant bands correspond to the Zn–O vibration.

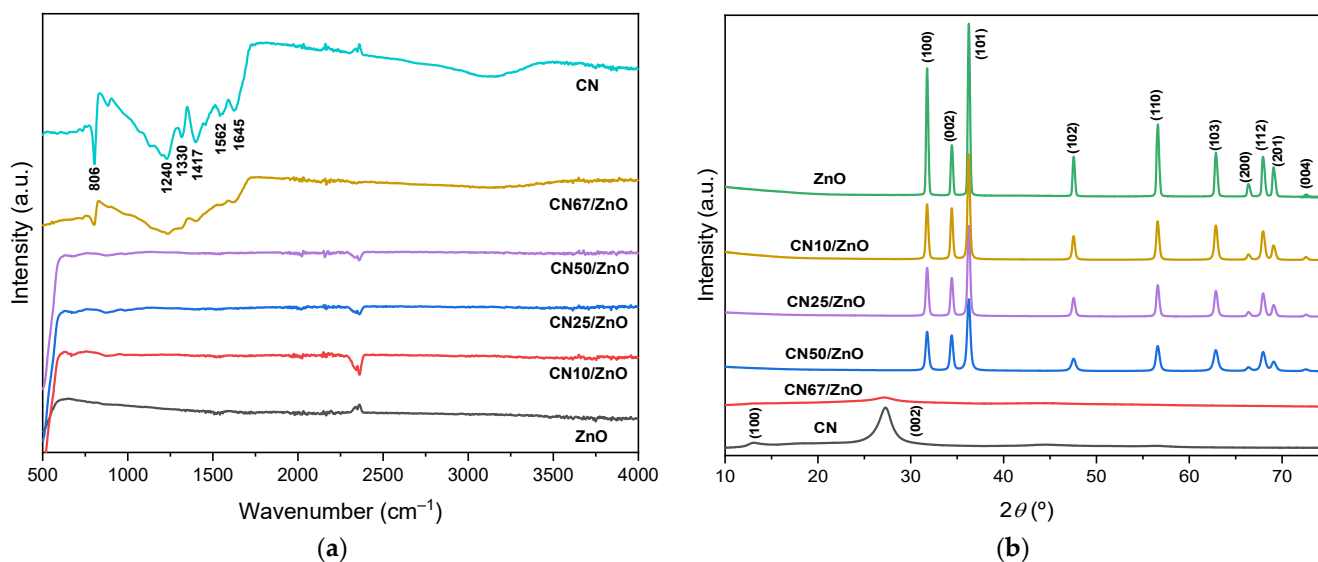


**Figure 1.** (a) FTIR spectra and (b) XRD patterns of pure CN, pristine ZnO, and CN/ZnO composites.

The crystallinity of the different prepared materials was studied by XRD. The XRD patterns of pure CN, pristine ZnO, and their corresponding composites are depicted in Figure 1b, while the average size of ZnO crystallites ( $d_{\text{ZnO}}$ ) is collected in Table 1. The CN sample presented the typical diffraction peaks at  $2\theta \sim 12.7$  and  $27.2^\circ$  due to (100) and (200) planes of the structural packing of tris-triazazine units and the interlayer stacking of  $g\text{-C}_3\text{N}_4$  aromatic units, respectively [45]. On the other hand, pristine ZnO and CN/ZnO composites with  $g\text{-C}_3\text{N}_4$  contents up to 50 wt% showed major diffraction peaks at  $2\theta$  values of  $31.7$ ,  $34.4$ ,  $36.2$ ,  $47.5$ ,  $56.6$ ,  $62.8$ ,  $66.2$ ,  $67.9$ ,  $69.0$ ,  $72.3$ , and  $77.1^\circ$ , which were associated with the lattice

planes of (100), (002), (101), (102), (110), (103), (200), (112), (201), and (004), respectively, corresponding to the formation of the ZnO wurtzite structure [46]. The intensity of the XRD peaks associated with the wurtzite phase was smaller with the increase of the weight ratio of melamine. During the precursor mixtures, these peaks completely disappear for the composite synthesized with the highest g-C<sub>3</sub>N<sub>4</sub> content, i.e., for CN67/ZnO (Figure 1b). The disappearance of the XRD peaks which belongs to the ZnO phase was already reported for CN/ZnO composites with g-C<sub>3</sub>N<sub>4</sub> contents around 50 wt% [26–28]. It seems that above this critical percentage the C<sub>3</sub>N<sub>4</sub> polymeric network hinders the formation of crystalline ZnO particles. Similar results were found for titania/carbon composites. The organic phase certainly avoided the formation of inorganic crystalline structures or even, phase transitions, at metal oxide contents between 15–85% due to the interactions between the different phases along the synthesis procedure [47]. On the other hand, the addition of g-C<sub>3</sub>N<sub>4</sub> in the ZnO phase had a clear effect on the crystallite size ( $d_{\text{ZnO}}$ , Table 1). Therefore, the lower the crystal size, the higher the g-C<sub>3</sub>N<sub>4</sub> content.

**Table 1.** Textural, chemical, and optical properties of pure CN, pristine ZnO, and CN/ZnO composites.

Samples	$d_{\text{ZnO}}$ (nm)	$S_{\text{BET}}$ (m <sup>2</sup> g <sup>-1</sup> )	$V_{\text{meso}}$ (cm <sup>3</sup> g <sup>-1</sup> )	$V_{\text{total}}$ (cm <sup>3</sup> g <sup>-1</sup> )	pH <sub>PZC</sub>	$E_g$ (eV)
CN	-	18	0.04	0.07	6.3	2.65
ZnO	32.3	<5	-	-	7.5	3.00
CN10/ZnO	28.1	11	0.09	0.17	7.4	3.10
CN25/ZnO	26.3	21	0.19	0.26	7.2	3.10
CN50/ZnO	21.8	29	0.03	0.23	7.1	3.15
CN67/ZnO	-	32	0.09	0.12	7.0	2.70

$S_{\text{BET}}$ : BET surface area;  $d_{\text{ZnO}}$ : Average crystal size;  $V_{\text{meso}}$ : Mesopore volume;  $V_{\text{total}}$ : Total pore volume; pH<sub>PZC</sub>: pH at the point of zero charge;  $E_g$ : Band gap energy.

The morphology of the samples was studied by SEM. Figure 2 shows the corresponding micrographs of pure CN, pristine ZnO, and selected CN/ZnO composites. The structure of bare CN consisted of pillared aggregates with irregular particles (Figure 2a), while particles in the range of 1–1.5 μm with hexagonal pyramid morphology were formed for pristine ZnO (Figure 2f). It is well-known that ZnO can be obtained into a large variety of morphologies, such as nanowires, nanorods, tetrapods, nanobelts, nanoflowers, and nanoparticles depending on the synthesis conditions. Under the one-pot synthesis procedure, wurtzite ZnO hexagonal micro-pyramids were majorly obtained. Nevertheless, this morphology strongly changes in the composites, which demonstrated the interactions of both precursors during the calcination treatments. With only 10 wt% of CN in the composite, the morphology was composed by sphere-like particles (Figure 2b), although a trend to form particle agglomerates can be identified as the g-C<sub>3</sub>N<sub>4</sub> content increased. Of note, the coral-like structure of 3D interconnected ZnO particles for CN25/ZnO, in which well-defined sphere-like particles were clearly identified (Figure 2c,d). With regards to CN50/ZnO, the morphology of the composite resembles again the structure of pure CN (Figure 2e). In general, all of the composites exhibited the g-C<sub>3</sub>N<sub>4</sub> structure embedded into ZnO. In addition, the crystal size of spherical ZnO particles was smaller with the increase in the wt% of g-C<sub>3</sub>N<sub>4</sub> content, in agreement with the XRD results. Therefore, the C<sub>3</sub>N<sub>4</sub> phase hinders the ZnO crystal growth and sintering, in a way that the pyramidal morphology of the ZnO particles was never observed in the composites, independently of the ratio between the phases. This fact is more notorious in CN67/ZnO, where the XRD peaks corresponding to ZnO were not observed (Figure 1), denoting the formation of very small nanocrystals or even, the amorphous character of these particles into the composite.

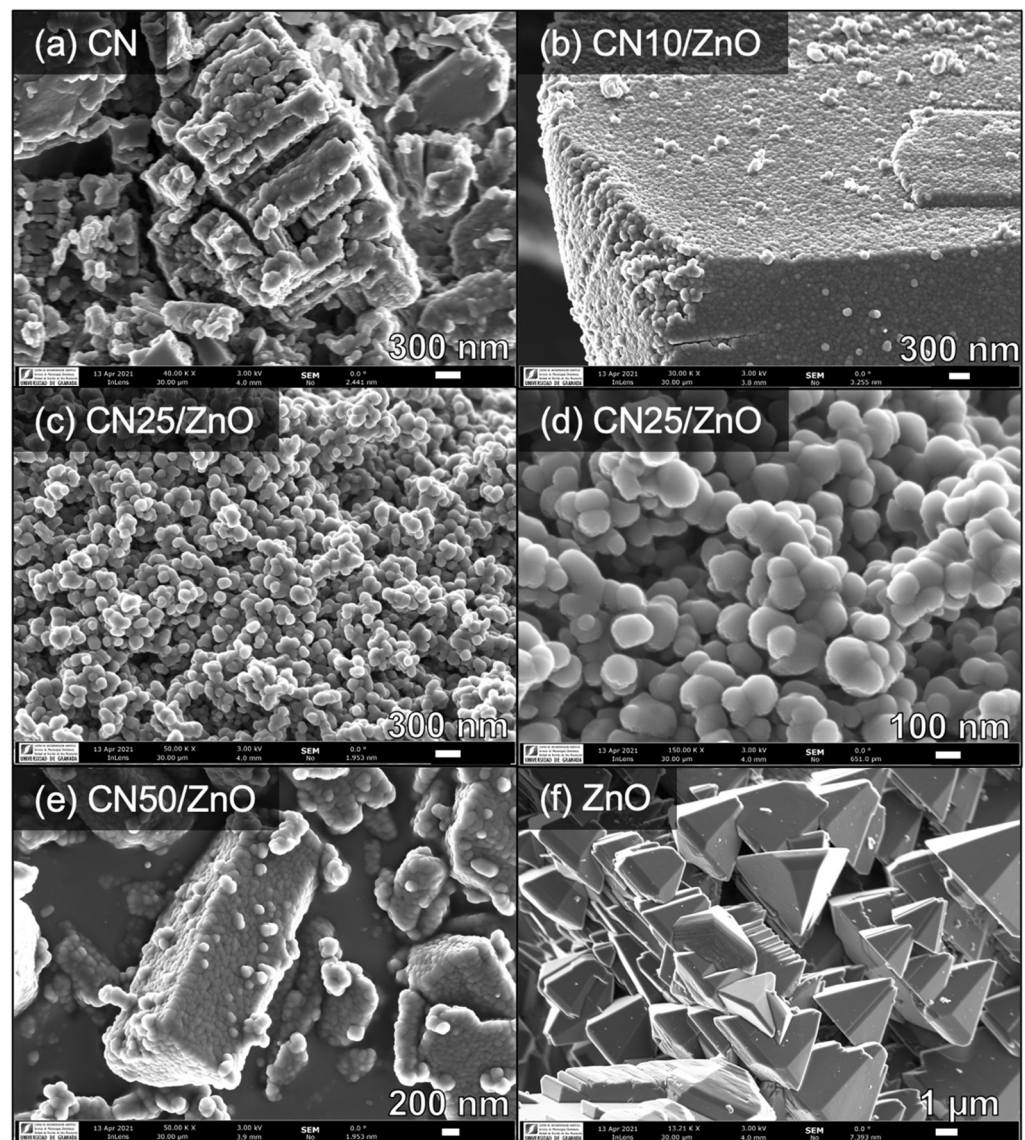


**Figure 2.** SEM micrographs of (a) pure CN, (b) CN10/ZnO, (c,d) CN25/ZnO, (e) CN50/ZnO, and (f) pristine ZnO.

The textural characterization of the different prepared materials was studied by the physical adsorption of nitrogen at  $-196\text{ }^{\circ}\text{C}$ . Figure 3 shows the  $\text{N}_2$  adsorption–desorption isotherms of pure CN and CN/ZnO composites. In general, all of the adsorption isotherms can be classified as type-II and type-IV, in concordance with the IUPAC classification, which indicates the presence of macroporosity or low porosity [26], and mesoporosity [48], respectively. Of note, the absence of micropores in all of the samples was negligible, since the adsorbed volume of  $\text{N}_2$  was recorded at low relative pressures. Nevertheless, the presence of large mesopores was notorious in most of the samples, in particular when a 25–50 wt% of  $\text{g-C}_3\text{N}_4$  was used in the composites (Figure 3c,d). This fact was denoted by the high  $\text{N}_2$  volume adsorbed at high relative pressures, as a consequence of the capillary condensation in mesopores. On the other hand, all of the samples showed a small type-H3 hysteresis loop due to aggregates formed by plate-like particles or adsorbents with slit-shaped pores [27,36].

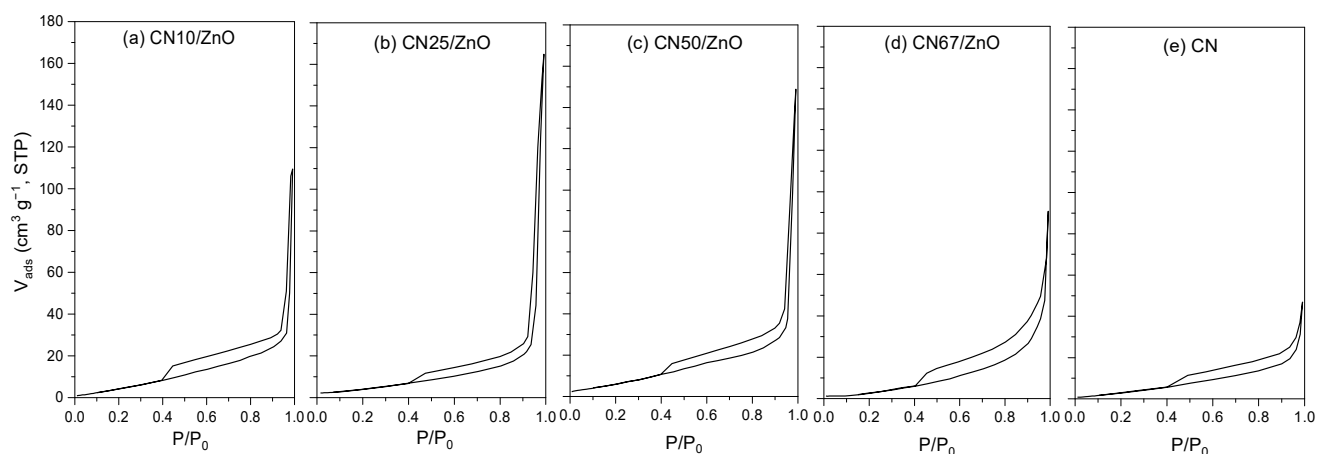


**Figure 3.** N<sub>2</sub> adsorption–desorption isotherms of (a) CN10/ZnO, (b) CN25/ZnO, (c) CN50/ZnO, (d) CN67/ZnO and (e) pure CN.

All of the synthesized materials exhibited a low BET surface area ( $S_{\text{BET}}$ ) in the range of 11 and 32 m<sup>2</sup> g<sup>−1</sup>, due to the absence of micropores. In general, CN/ZnO composites usually show slightly higher  $S_{\text{BET}}$  values than pure CN (e.g., 18 and 29 m<sup>2</sup> g<sup>−1</sup> for pure CN and CN50/ZnO, respectively) and pristine ZnO (<5 m<sup>2</sup> g<sup>−1</sup>). The addition of any amount of g-C<sub>3</sub>N<sub>4</sub> allowed for the enhancement of the porosity of the composites due to the development of mesoporosity. Therefore, the mesopore volume ( $V_{\text{meso}}$ ) and total pore volume ( $V_{\text{total}}$ ) increased as the g-C<sub>3</sub>N<sub>4</sub> content increased and reached their maximum values of around 25–50 wt% (e.g.,  $V_{\text{meso}} = 0.19$  and 0.09 cm<sup>3</sup> g<sup>−1</sup> for CN25/ZnO and CN67/ZnO, respectively). These results are in agreement with the reported studies in literature [27] and those obtained by SEM, in which a more porous structure can be identified for the CN25/ZnO composite.

The surface chemical composition of pure CN, pristine ZnO, and CN/ZnO composites was investigated by XPS (Figure S1a and Table S1). The high resolution C1s spectra of all g-C<sub>3</sub>N<sub>4</sub>-based materials can be deconvoluted in three peaks (Figure 4a). The main peak located at ~284.8 eV was assigned to N–C=N bonds from C-sp<sup>2</sup> atoms bonded to nitrogen in aromatic rings, while the second peak at ~286.2 eV corresponds to C-sp<sup>3</sup> atoms from C–(N)<sub>3</sub> bonds [27]. The last peak placed at ~288.2 eV was attributed to C–N–C bonds [49]. The C1s region was comparable for all of the CN/ZnO composites. However, it is noteworthy to mention the strong change in the C1s profiles (carbon nature) from pure CN to the derivative composites. In bare CN, the large part of C–bonds corresponds to C–N–C structures, which in the presence of the ZnO phase are transformed into N–C=N bonds (Figure 4a), indicating an increase of the aromaticity in the g-C<sub>3</sub>N<sub>4</sub> phase. This fact is related with a re-ordering of the g-C<sub>3</sub>N<sub>4</sub> structure, as a consequence of the presence of large amounts of ZnO and the post-treatment in air. In fact, a very small shoulder at ~283 eV seems to be identified for CN/ZnO composites with g-C<sub>3</sub>N<sub>4</sub> below 50 wt% and corresponding to Zn–C bonds due to oxygen vacancies ( $O_{\text{vac}}$ ) formed in the ZnO structure [50,51]. The occurrence of  $O_{\text{vac}}$  has been reported to have an enhancement in the visible light response of the materials [52]. Concerning the O1s region, the high resolution spectra were deconvoluted in two main contributions (Figure 4b), the first peak located at ~530.5 eV was assigned to  $O_2^-$  ions in Zn–O bonds of the ZnO wurtzite structure, while the peak at ~532 eV corresponds to OH groups absorbed onto the ZnO surface [22,27,53]. By comparing the O1s regions of pristine ZnO and CN/ZnO composites, a similar nature of the Zn–O bonds is obtained since the profiles of the spectra are maintained. However, a clear shift is also observed towards higher binding energies (BE), indicating a lower electronic density of the ZnO phase, which is probably associated with the electron transfers between phases or even, a certain reduction of the surface oxygen with the formation of  $O_{\text{vac}}$  [50]. The proportion of  $O_2^-$  groups progressively increased as the g-C<sub>3</sub>N<sub>4</sub> content increased (Table S1). The N1s spectra were similar for all of the g-C<sub>3</sub>N<sub>4</sub>-based materials and were

deconvoluted in three main contributions at  $\sim 398.7$ ,  $\sim 400.0$ , and  $\sim 401.2$  eV attributed to  $N-sp^2$  (C–N=C bonds) in the triazine rings, tertiary nitrogen atoms from  $NV(C)_3$  bonds, and amino groups (C–N–H) (Figure S1b) [49]. Regarding the Zn2p region, only a  $Zn2p_{3/2}$  peak at  $\sim 1021.2$  eV associated with a  $Zn^{2+}$  oxidation state was found for all of the samples containing ZnO (Figure S1c) [22,27]. The BE difference between  $Zn2p_{3/2}$  and  $Zn2p_{1/2}$  was always maintained at 23.0 eV. However, a shift towards lower BE is observed for CN/ZnO composites with  $g-C_3N_4$  below 50 wt%. This transition occurred by a heterojunction formed between both  $g-C_3N_4$  and ZnO phases [50]. Of note, the analysis of the different spectral regions pointed out the stronger similarity of CN67/ZnO with the pure phases, indicating smaller interactions between the phases in this sample. These results point out that the formation of heterojunctions between both semiconductors is favored at  $g-C_3N_4$  contents below 50 wt%.

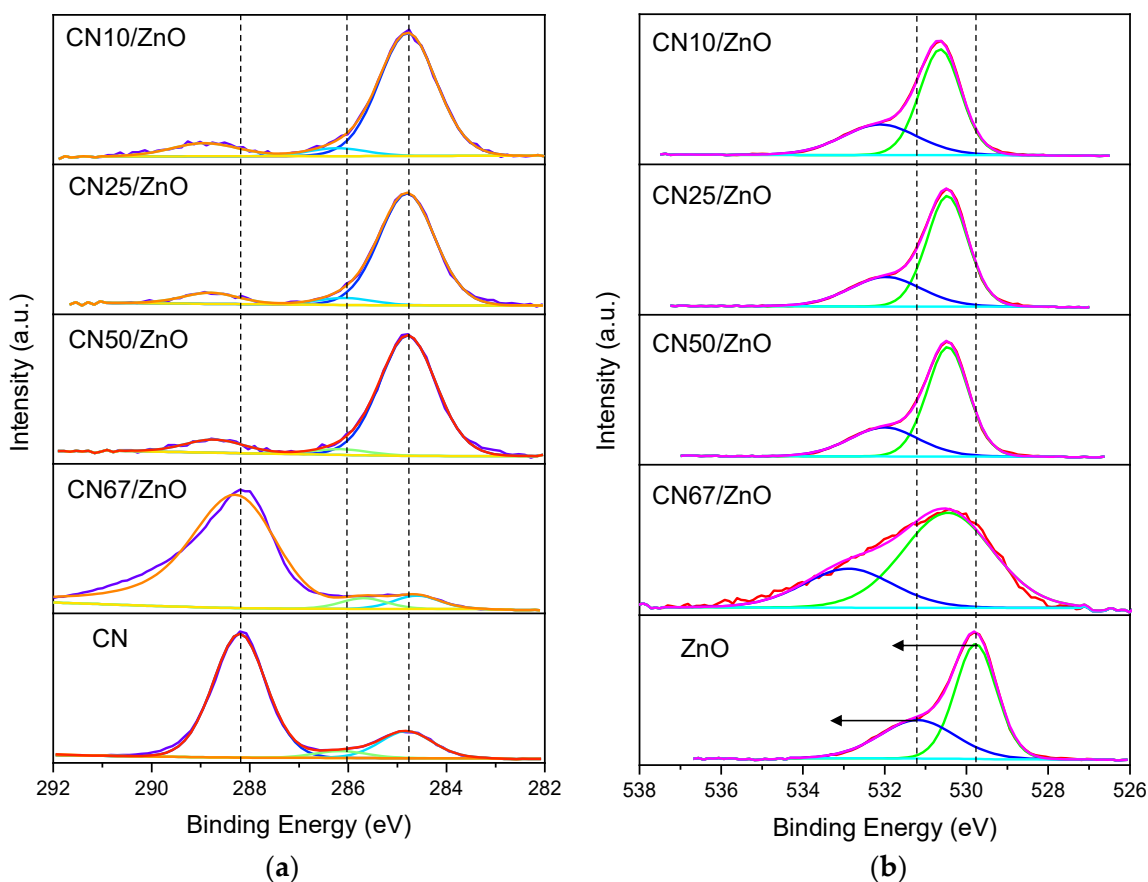


**Figure 4.** XPS spectra and deconvolution of (a) C1s and (b) O1s regions of CN/ZnO composites. Pure CN and pristine ZnO are also plotted for comparison.

The UV–Vis diffuse reflectance spectra of pure CN and CN/ZnO composites, expressed in terms of Kubelka–Munk absorption units, are depicted in Figure 5a. With regards to all of the composites, a strong intensive absorption band was observed in the UV range with onset at  $\lambda < 400$  nm, associated with common UV–Vis absorption of pristine ZnO, as previously reported [22]. For the CN material, it also shows a band in the visible range due to  $\pi-\pi^*$  transitions of conjugated ring system [54]. Regarding the ZnO spectrum, an enhanced absorption in the UV range can be observed with the incorporation of  $g-C_3N_4$  in the corresponding composites. Figure 5b exhibits the Tauc's plots vs. the energy (eV). The calculated  $E_g$  of pure CN and pristine ZnO was 2.65 and 3.0 eV, respectively, which are comparable values to those reported in literature [8]. Nevertheless, when the band gaps of CN/ZnO composites were analyzed, different results were found depending on the  $g-C_3N_4$  content. Therefore, the  $E_g$  value was around 2.70 eV, which is close to the pure CN,

at high  $g\text{-C}_3\text{N}_4$  contents (sample CN67/ZnO), while with the increasing ZnO content, the band gap became even higher than for pure ZnO, which is between 3.10–3.15 eV (Table 1). The presented CN and CN67/ZnO developed adsorption at  $\lambda > 375$  nm, while with the increasing ZnO ratio in the composite, a clear enhanced UV-absorption in the range of 300–400 nm is evident. These results should be due to the interactions between both phases and their transformations during the synthesis procedure, as aforementioned, which are related to the quantum size of active nanoparticles and/or electronic interphase effects. As previously mentioned, the higher the  $g\text{-C}_3\text{N}_4$  content in the composite, the smaller the interactions between the phases.

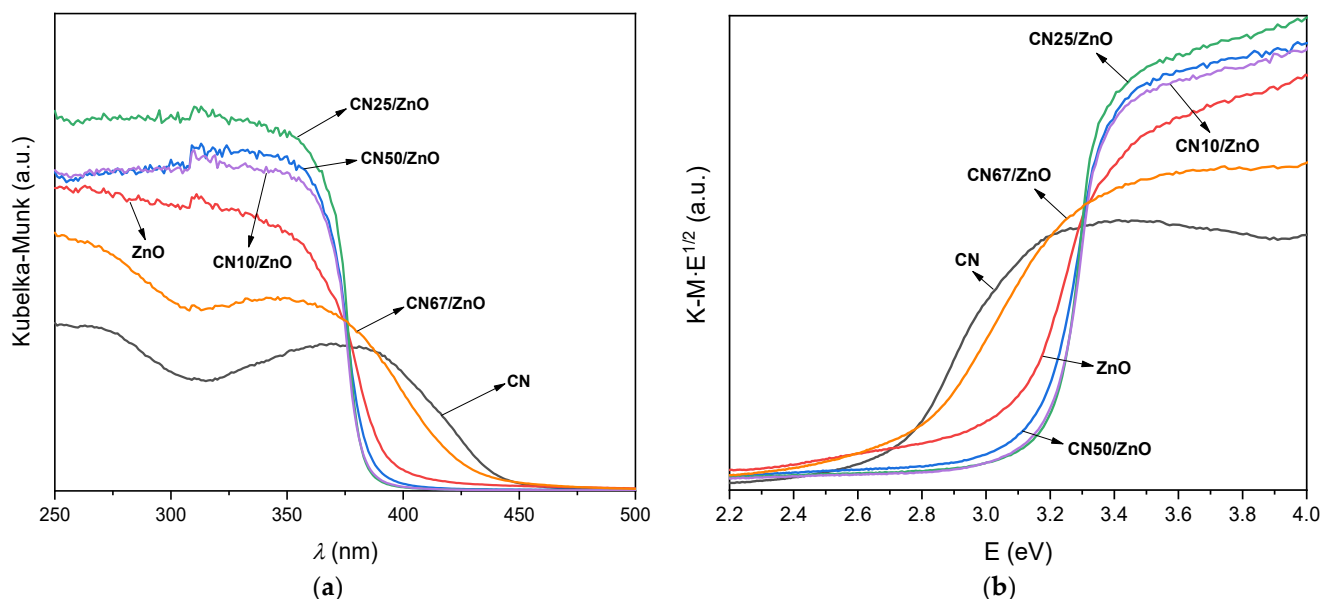


**Figure 5.** (a) UV-Vis spectra and (b) Tauc's plots vs. energy (eV) of pure CN, pristine ZnO, and CN/ZnO composites.

### 3.2. Photocatalytic Degradation of 5-FU under UV-LED Irradiation

The photocatalytic performance of pure CN, pristine ZnO, and CN/ZnO composites (with different  $g\text{-C}_3\text{N}_4$  contents) for the 5-FU degradation at natural pH under UV-LED irradiation, is shown in Figure 6. The kinetic rate constant ( $k'_{ap}$ ), the 5-FU conversion ( $X_{5-FU}$ ), coefficient of variation ( $k_{CV}$ ), and regression coefficient ( $r^2$ ) are summarized in Table 2. The photolysis reaction corroborated the resistance of 5-FU for degradation ( $X_{5-FU} < 5\%$ ) and its light-stability in the absence of any photocatalyst. On the other hand, the adsorption-desorption equilibrium in dark phase experiments was established after 60 min for the prepared catalysts. The adsorption capacity was 3.0%, 4.7%, 1.5%, 14.3%, 9.6%, and 5.5% for CN, ZnO, CN67/ZnO, CN50/ZnO, CN25/ZnO, and CN10/ZnO, respectively. In general, the adsorption capacity of the materials was well-correlated with the porous texture (e.g., SBET), taking into account the comparable neutral surface chemistry of the samples. However, the CN50/ZnO composite presented the highest 5-FU removal by adsorption. This could be due to the presence of very small pores or micropores ( $V_{total} - V_{meso}$ ), which present the largest affinity by the pollutant molecules.

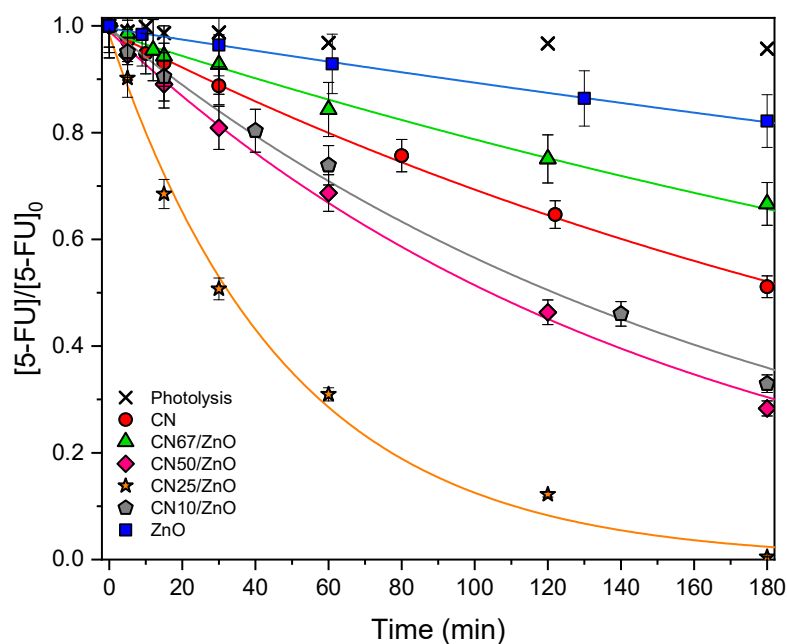


**Figure 6.** Photocatalytic degradation of 5-FU at natural pH as a function of time for pure CN, pristine ZnO, and CN/ZnO composites. Curves represent the fitting of the pseudo-first order equation to the experimental data.

**Table 2.** The 5-FU conversion after 180 min ( $X_{5-FU}$ ), pseudo-first order kinetic rate constant ( $k'_{ap}$ ), coefficient of variation ( $k_{CV}$ ), and regression coefficient ( $r^2$ ) of 5-FU.

Catalyst	pH	Scavenger	$X_{5-FU}$ (%)	$k'_{ap}$ ( $10^{-3} \text{ min}^{-1}$ )	$k_{CV}$ (%)	$r^2$
Photolysis	6.3	none	4.3	-	-	-
CN	6.3	none	48.9	3.6	2.3	0.997
ZnO	6.3	none	17.8	1.1	2.1	0.998
CN10/ZnO	6.3	none	67.1	5.7	4.4	0.993
CN25/ZnO	6.3	none	100.0	20.6	6.7	0.994
CN50/ZnO	6.3	none	71.7	6.5	3.2	0.997
CN67/ZnO	6.3	none	33.3	2.2	3.1	0.995
CN25/ZnO	3.0	none	48.3	4.0	3.5	0.995
CN25/ZnO	9.0	none	91.3	11.6	4.3	0.996
CN25/ZnO	6.3	MeOH	56.6	4.5	5.4	0.98
CN25/ZnO	6.3	EDTA	66.8	7.0	8.8	0.978
CN25/ZnO	6.3	FFA	56.3	4.6	3.7	0.995

Analyzing the performance of pristine phases, CN is more active than ZnO according to the higher BET surface area and pore volume and a narrower Eg was detected, taking into account the comparable UV absorption under the UV-LED used in the photocatalytic experiments. Nevertheless, the activity in the composites is not directly related with the g-C<sub>3</sub>N<sub>4</sub> content, which denotes the importance of fitting compositions and physicochemical characteristics along the synthesis procedure. In general, the presence of ZnO in the composites leads to a higher efficiency for the 5-FU degradation under UV-LED irradiation in comparison with both pure CN and pristine ZnO, denoting a clear effect of the synergism between the phases. In fact, the lower photocatalytic activity was obtained for the lowest ZnO content, CN67/ZnO composite (i.e., 33.3 wt% ZnO), increasing the activity as the ZnO content up to 75% (i.e., CN25/ZnO). However, the CN10/ZnO composite (i.e., 90 wt% ZnO) showed a clear effect of over-doping, which leads to a decrease of activity regarding CN25/ZnO. However, it was clearly not only more active than pristine ZnO, but also than pure CN. As indicated, CN25/ZnO presented the best performance

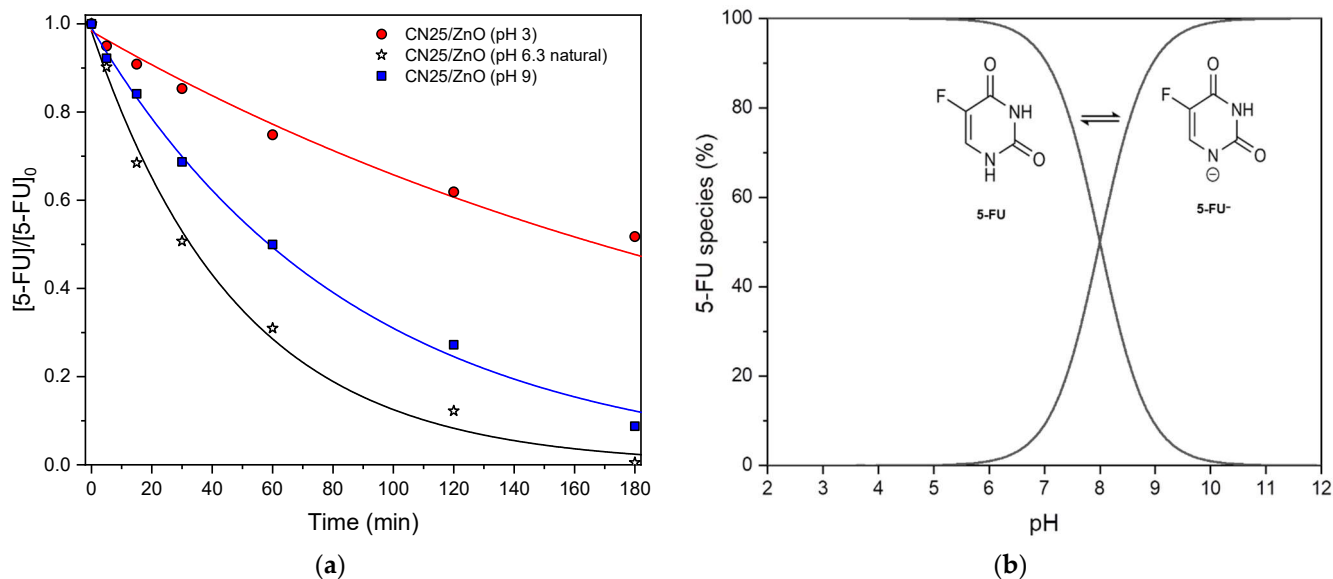
among all of the composites, which was due to an adequate combination of composition, morphology, homogeneity, and enhanced porous texture (this sample presented the highest mesopore volume), intermediate crystal size, and strong interaction between phases, which significantly influence on heterojunctions formation inducing changes in separation photogenerated charges and consequently, on the photocatalytic activity [28,55].

The mineralization degree of the different materials was studied for the photodegradation of 5-FU. Therefore, TOC reduction was also determined at the end of the photocatalytic experiments for the different catalysts under UV-LED irradiation (180 min). In general, the level of mineralization exhibited a similar trend to what was observed for the 5-FU conversion, i.e., CN67/ZnO, CN50/ZnO, CN25/ZnO, CN10/ZnO, CN, and ZnO led to TOC reductions of 15%, 31%, 48%, 27%, 18%, and 8%, respectively, under UV-LED irradiation.

The most active photocatalyst, i.e., CN25/ZnO composite, was selected for the study of different operating parameters and the photocatalytic mechanism.

### 3.2.1. Influence of pH Value on 5-FU Degradation

The solution pH in the photocatalytic experiments affects the surface charge properties of the catalyst, the charge of pollutants, the adsorption onto the photocatalyst surface, the size of aggregate particles formed, as well as the concentration of radical species. Therefore, the effect of initial pH values for the degradation of 5-FU was evaluated in the pH range from 3.0 to 9.0, taking as reference the previously discussed experiments carried out at natural pH (i.e., 6.3), under UV-LED irradiation for the CN25/ZnO photocatalyst (Figure 7a). The respective pseudo-first order kinetic rate constant ( $k'_{ap}$ ), coefficient of variation ( $k_{CV}$ ), and regression coefficient at different pH values can be also found in Table 2. Of note, a slight decrease in the pH value was observed after the photocatalytic experiments (around 0.5).



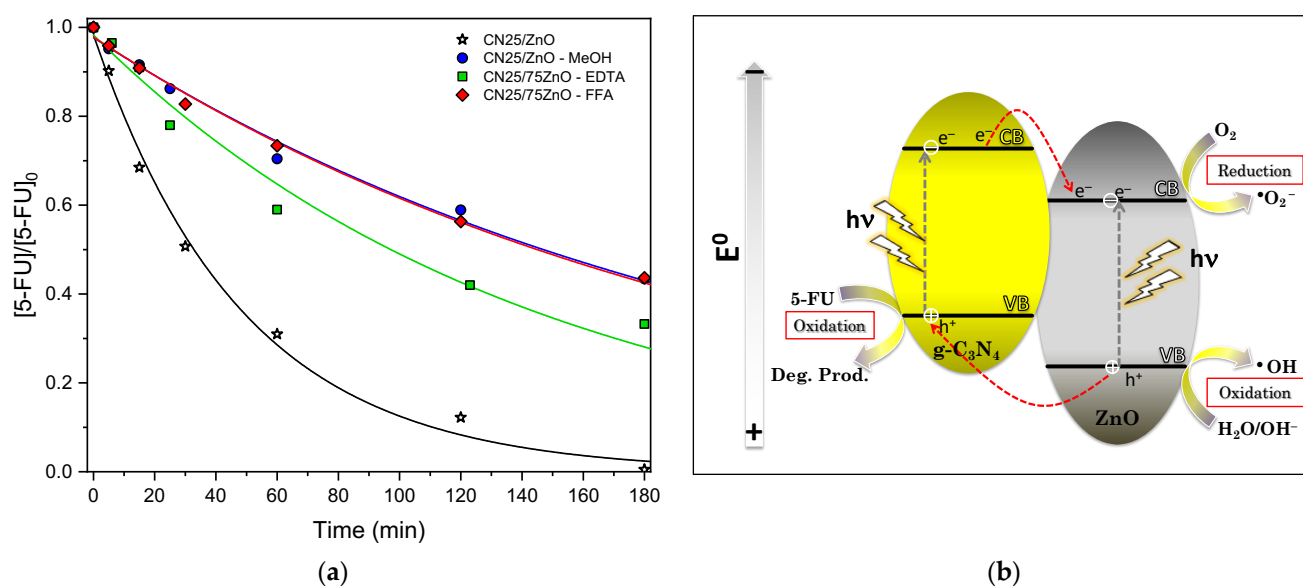
**Figure 7.** (a) Normalized concentration of 5-FU as a function of time pH values of 3.0, 6.3 (natural pH), and 9.0 for CN25/ZnO. (b) The 5-FU species distribution diagram as a function of pH.

Figure 7b shows the species distribution diagram of 5-FU as a function of pH. The diagram exhibits the equilibrium between the neutral (5-FU) and deprotonated form of 5-FU (anionic 5-FU<sup>-</sup>). The neutral form of 5-FU predominates below pH 8.0 and the deprotonated form (5-FU<sup>-</sup>) is mainly observed above pH 8.0 [56]. On the other hand, the  $pH_{PZC}$  of the composites is in the range of 7.0–7.4, which indicates that the composite surface is positively or negatively charged for lower or higher pH values, respectively. In this context, the obtained results indicate that the highest photocatalytic activity of the composites is obtained at natural pH values, since the 5-FU removal increased as the media pH value from

pH 3.0 to 6.3 (48.3% and 100.0%, respectively). In this situation, the 5-FU molecules remain neutral (uncharged), while the catalyst surface is slightly negatively charged. Therefore, the adsorption is mostly governed by the  $\pi$ - $\pi$  interactions of the aromatic structures, which were enhanced with the presence of ZnO, in agreement with the XPS results. The lowest activity obtained at pH 3.0 should be related with the agglomeration of the photocatalyst particles and a reduction of the available surface area [57], as well as the presence of chlorine species (from HCl added to adjust the pH value), that can compete with the pollutant molecules for the generated oxidative species [58]. On the contrary, at pH 9.0, both the CN25/ZnO photocatalyst and the 5-FU molecules are negatively charged ( $pK_a = 8.0$ ) and electrostatic repulsions occur, explaining the lower 5-FU conversion obtained at basic pH value. However, a higher 5-FU conversion was obtained at pH 9.0 when compared with pH 3.0. These results can be due to the presence of hydroxyl anions which can lead to the formation of hydroxyl radicals through the reaction with positive holes, resulting in an enhancement of the photocatalytic performance [59,60].

### 3.2.2. Photocatalytic Degradation Pathway and Reaction Mechanism

MeOH, FFA, and EDTA were used as scavengers for radicals, non-radicals (singlet oxygen), and holes, respectively, in order to study the possible reactive oxygen species (ROS) involved in the photodegradation of 5-FU under UV-LED irradiation (Figure 8a).



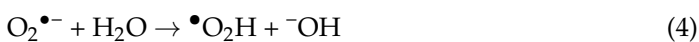
**Figure 8.** (a) Effect of radical/hole/non-radical scavengers (MeOH/EDTA/FFA) on the photocatalytic degradation of 5-FU using the CN25/ZnO composite. (b) Scheme of the tentative photocatalytic mechanism with CN/ZnO composites.

Figure 8a shows that all of the scavengers added to the reaction fulfilled their role and decreased the 5-FU degradation after 180 min of UV-LED irradiation. In particular, this effect was more pronounced in the presence of MeOH and FFA and to a lesser extent by EDTA, the 5-FU photodegradation was around 56.6%, 56.3%, and 66.8%, respectively, compared with 100% of 5-FU degradation in the absence of any scavenger (Table 2). The results suggest that the radicals (mainly hydroxyl radicals) and non-radical species such as, singlet oxygen appear to be the main responsible active species in the degradation of 5-FU, while photogenerated holes play a secondary role in the 5-FU photodegradation [27].

An additional experiment with the CN25/ZnO composite was carried out to study the role of the dissolved oxygen in the generation of ROS involved in the mechanism reaction. In this context, the degradation of 5-FU was studied by changing the pure gas from oxygen to nitrogen, i.e., from reactive and inert atmospheres (Figure S2, Supplementary Materials). The photocatalytic activity with nitrogen purge was almost half compared

with the oxygen flow (i.e., 54.9% vs. 100%, respectively), which demonstrated the marked influence of dissolved oxygen in the generation of ROS for the 5-FU degradation under UV-LED irradiation.

Taking into consideration the ROS active in the photocatalytic reactions, the physico-chemical properties of the CN/ZnO composites and based on the related literature, a tentative photocatalytic mechanism is proposed in Figure 8b. The g-C<sub>3</sub>N<sub>4</sub> is a typical visible light-driven photocatalyst, although a certain UV absorption under near UV-LED irradiation was observed (Figure 5b). As known, the conduction band (CB) potential of pure g-C<sub>3</sub>N<sub>4</sub> is more negative than the pristine ZnO (i.e., −1.12 V vs. −0.5 V, respectively) [27,32,61]. Therefore, the electrons may be excited to CB of pure g-C<sub>3</sub>N<sub>4</sub>, while holes are generated in the corresponding valance band (VB). Thereafter, the photogenerated electrons are transferred to CB of pristine ZnO, as a consequence of the heterojunction interface produced during the thermal treatment. Of note, the generated holes into g-C<sub>3</sub>N<sub>4</sub> are not able to directly oxidize <sup>−</sup>OH or H<sub>2</sub>O into <sup>•</sup>OH, due to the fact that its VB edge potential is less positive compared with the standard redox potential of <sup>−</sup>OH/<sup>•</sup>OH (2.38 V) or H<sub>2</sub>O/<sup>•</sup>OH (1.99 V) [62,63]. However, they can oxidize the 5-FU molecules into degradation products. On the other hand, ZnO can be also excited upon irradiating the composite. In this case, the corresponding holes generated in its VB are able to form <sup>•</sup>OH radicals and/or be transferred to the VB of g-C<sub>3</sub>N<sub>4</sub> [64]. Therefore, a separation of the photogenerated charge carriers was achieved, while holes or electrons can react with water or dissolved oxygen to yield hydroxyl or superoxide radicals, respectively, and consequently, degrading the 5-FU molecules as follows:



### 3.2.3. Reutilization Tests

The photostability of the CN25/ZnO composite was assessed in several consecutive reusability cycles under UV-LED irradiation for 180 min (Figure 9 and Table 2). The experimental procedure was described in Section 2.3. However, after each reaction, the photocatalyst was washed with distilled water and dried at 60 °C overnight. The resulting catalyst was reused in the photocatalytic reactions using a fresh 5-FU solution. The 5-FU conversion values decreased slightly between the first and third run (from 100.0% to 86.9%). However, the photocatalytic activity remained practically constant after the third and fourth cycles (86.9% and 85.8%, respectively). This small deactivation could be related with the chemisorption of 5-FU molecules or reaction intermediates on the stronger active sites of the photocatalyst, remaining after the saturation of the available sites for consecutive reactions. The results showed that the composite can be used to stabilize ZnO in photodegradation processes. Evidently, in this case, there was no photo corrosion, as the photocatalyst exhibited good photostability and performance to remove 5-FU under UV-LED irradiation, even after 12 h of use [26,28,32].

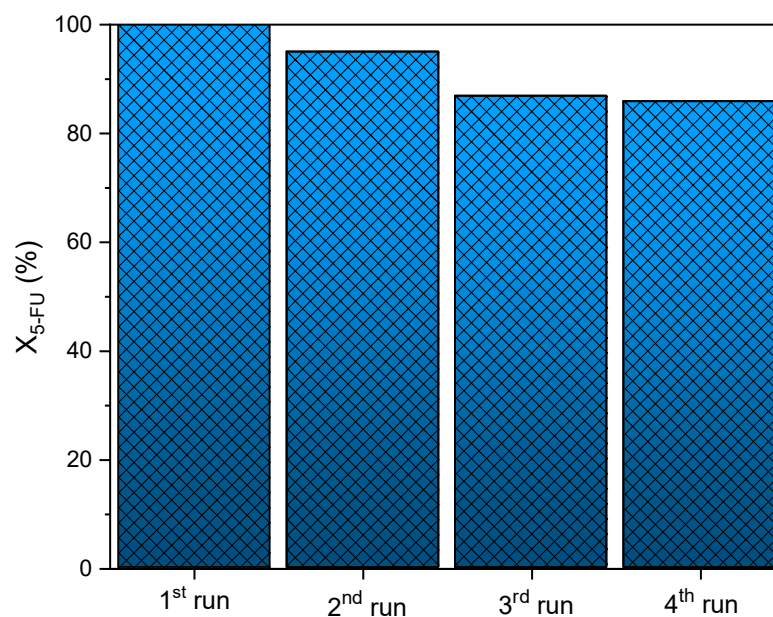


**Figure 9.** Reusability of CN25/ZnO photocatalyst for the 5-FU degradation during four consecutive cycles.

Table 3 summarizes the results obtained in this work with those reported in literature. Some experimental details, such as the procedure synthesis, the precursors, the pollutant studied, the light source employed, and the pollutant removal at a determined time are listed. The results obtained with the best photocatalyst, i.e., CN25/ZnO, are in agreement with the values reported in the literature, although the similarity as well as the difference can be observed.

**Table 3.** Compilation of recently published works regarding g-C<sub>3</sub>N<sub>4</sub>/ZnO composites for the photodegradation of pollutants in aqueous solution.

Material	Synthesis	C <sub>3</sub> N <sub>4</sub> /ZnO Precursors	Pollutant	Light Source	Removal (%) / Time (Min)	Ref.
C-doped g-C <sub>3</sub> N <sub>4</sub> /ZnO	Sol-gel + calcination	Dicyandiamide zinc nitrate	MB (10 mg L <sup>-1</sup> )	Xe lamp	78.6/120	[26]
Mesoporous g-C <sub>3</sub> N <sub>4</sub>	Impregnation + calcination	Melamine zinc nitrate	MO (10 mg L <sup>-1</sup> )	W lamp	90.8/120	[27]
C <sub>3</sub> N <sub>4</sub> /ZnO	Mechanical milling + calcination	Melamine zinc oxide	MB (0.01 mM)	Fluorescent lamp Xe lamp	~90.0/180 ~85.0/180	[30]
ZnO/g-C <sub>3</sub> N <sub>4</sub> nanofibers	Calcination + electrospinning	Melamine zinc acetate	MB (0.01 mM)	Xe lamp	91.8/120	[31]
g-C <sub>3</sub> N <sub>4</sub> /ZnO pencil-like	Calcination + hydrothermal + chemical deposition	Melamine zinc acetate	RhB (7.5 mg L <sup>-1</sup> )	Visible (λ > 420 nm)	94.0/120	[32]
ZnO/g-C <sub>3</sub> N <sub>4</sub>	Sol-gel + calcination	Melamine zinc acetate	AML (10 mg L <sup>-1</sup> )	Fluorescent lamps	53.0/400	[28]
g-C <sub>3</sub> N <sub>4</sub> /ZnO nanorods	Calcination + sol-gel + hydrothermal	Melamine zinc acetate	MO (20 mg L <sup>-1</sup> )	Xe lamp	85.7/30	[65]
CN/ZnO	Calcination	Melamine zinc nitrate	5-FU (154 mM)	LED-UV	100.0/180	This work

MB: Methylene blue; MO: Methyl orange; RhB: Rhodamine B; AML: Amiloride; 5-FU: 5-Fluorouracil.

#### 4. Conclusions

The easy one-pot thermal method used to synthesize the CN/ZnO composites favored coral-like structures of spherical particles of ZnO on the g-C<sub>3</sub>N<sub>4</sub> structure. The morphology of these composites depended markedly on the g-C<sub>3</sub>N<sub>4</sub> content, in which a homogenous distribution of nanoparticles was achieved preferentially up to 25 wt% of g-C<sub>3</sub>N<sub>4</sub>. The crystallite size of ZnO decreased contrary to the g-C<sub>3</sub>N<sub>4</sub> content, although the wurtzite

structure was identified in most of the composites. The porosity and surface area of the materials were low, although an enhancement of the mesoporosity was always favored with the  $g\text{-C}_3\text{N}_4$  addition. The main chemical functionalities identified in the CN/ZnO composites were mainly formed by N–C=N bonds, as a consequence of a re-ordering of the  $g\text{-C}_3\text{N}_4$  structure due to the presence ZnO and the thermal exfoliation in air. The shift of certain functionalities towards lower BE suggested the occurrence of a heterojunction interface between  $g\text{-C}_3\text{N}_4$  and ZnO phases, with these phase connections as well-established for CN/ZnO composites with a  $g\text{-C}_3\text{N}_4$  content below 50 wt%. All of the CN/ZnO composites showed higher light absorption in the UV range in comparison with the reference materials.

All of the synthesized CN/ZnO composites showed photocatalytic activity for the degradation of 5-FU under UV-LED irradiation. The best composite was prepared with 25 wt% of  $g\text{-C}_3\text{N}_4$  (i.e., CN25/ZnO) due to a smaller size and better distribution of ZnO crystallites on the  $g\text{-C}_3\text{N}_4$  structure, an enhanced mesoporosity, and heterojunction interface, which hinders or decreases the electron–hole recombination. The catalytic results obtained at different pH values confirmed that the 5-FU removal was enhanced at natural pH due to the  $\pi\text{-}\pi$  interactions established between the 5-FU molecules and the catalyst surface. The employment of different scavengers allowed for the elucidation of the ROS involved in the photocatalytic mechanism. Therefore, radicals (mainly hydroxyl radicals) and non-radical species (singlet oxygen) seem to be the main responsible active species in the degradation of 5-FU, while photogenerated holes play a secondary role. Furthermore, the occurrence of dissolved oxygen enhanced the photocatalytic activity of the composites due to the generation of ROS. In the tentative photocatalytic mechanism, the photogenerated holes in VB of ZnO under UV-LED are transferred to VB of  $g\text{-C}_3\text{N}_4$ , while its photogenerated electrons are transferred to CB of ZnO, as a consequence of the heterojunction interface produced during the thermal treatment of CN/ZnO composites.

Overall, CN25/ZnO showed high photostability and performance for the degradation of 5-FU during four consecutive reaction cycles.

**Supplementary Materials:** The following supporting information can be downloaded at: <https://www.mdpi.com/article/10.3390/nano12030340/s1>: Table S1: Percentages of species and corresponding binding energies (in brackets, eV) of pure CN, pristine ZnO, and the different CN/ZnO composites determined by XPS analysis; Figure S1: XPS spectra of pure CN, pristine ZnO, and the CN67/ZnO composite: (a) Survey, (b) N1s region, and (c) Zn2p region; Figure S2: Photocatalytic degradation of 5-FU with different types of purge gas (O<sub>2</sub> and N<sub>2</sub>) for the CN25/ZnO composite.

**Author Contributions:** Conceptualization, L.M.P.-M., S.M.-T. and F.J.M.-H.; investigation, Á.P.-M. and L.T.P.-P.; writing—original draft preparation, Á.P.-M., L.T.P.-P., S.M.-T. and L.M.P.-M.; writing—review and editing, Á.P.-M., L.T.P.-P., S.M.-T., L.M.P.-M. and F.J.M.-H.; supervision, L.M.P.-M., S.M.-T. and F.J.M.-H.; funding acquisition, L.M.P.-M., S.M.-T. and F.J.M.-H. All authors have read and agreed to the published version of the manuscript.

**Funding:** This work was financially supported by the Spanish Projects, ref. RTI2018-099224-B-I00 from MCIN/AEI/10.13039/501100011033/FEDER “Una manera de hacer Europa”, and ref. B-RNM-486-UGR20 supported by Junta de Andalucía.

**Institutional Review Board Statement:** Not applicable.

**Informed Consent Statement:** Not applicable.

**Data Availability Statement:** Not applicable.

**Acknowledgments:** Á.P.-M. is grateful to the Spanish MICIN/AEI/10.13039/501100011033 and the European Social Found (FSE) “El FSE invierte en tu futuro” for a predoctoral research contract (PRE2019-087946). S.M.-T. (RYC-2019-026634-I) and L.M.P.-M. (RYC-2016-19347) acknowledge the Spanish MICIN/AEI/10.13039/501100011033 and the European Social Found (FSE) “El FSE invierte en tu futuro” for their Ramón y Cajal research contracts. “Unidad de Excelencia Química Aplicada a Biomedicina y Medioambiente” of the University of Granada (UEQ—UGR) is gratefully acknowledged for the technical assistance.

**Conflicts of Interest:** The authors declare no conflict of interest.

## References

1. Silva, T.L.S.; Morales-Torres, S.; Esteves, C.M.P.; Ribeiro, A.R.; Nunes, O.C.; Figueiredo, J.L.; Silva, A.M.T. Desalination and removal of organic micropollutants and microorganisms by membrane distillation. *Desalination* **2018**, *437*, 121–132. [[CrossRef](#)]
2. Deblonde, T.; Cossu-Leguille, C.; Hartemann, P. Emerging pollutants in wastewater: A review of the literature. *Int. J. Hyg. Environ. Health* **2011**, *214*, 442–448. [[CrossRef](#)]
3. Kosjek, T.; Perko, S.; Zigon, D.; Heath, E. Fluorouracil in the environment: Analysis, occurrence, degradation and transformation. *J. Chromatogr. A* **2013**, *1290*, 62–72. [[CrossRef](#)]
4. Mukherjee, S.; Mehta, D.; Dhangar, K.; Kumar, M. Environmental fate, distribution and state-of-the-art removal of antineoplastic drugs: A comprehensive insight. *Chem. Eng. J.* **2021**, *407*, 127184. [[CrossRef](#)]
5. Zhang, J.; Chang, V.W.; Giannis, A.; Wang, J.Y. Removal of cytostatic drugs from aquatic environment: A review. *Sci. Total Environ.* **2013**, *445–446*, 281–298. [[CrossRef](#)]
6. Misik, M.; Filipic, M.; Nersesyanyan, A.; Kundi, M.; Isidori, M.; Knasmueller, S. Environmental risk assessment of widely used anticancer drugs (5-fluorouracil, cisplatin, etoposide, imatinib mesylate). *Water Res.* **2019**, *164*, 114953. [[CrossRef](#)] [[PubMed](#)]
7. Negreira, N.; de Alda, M.L.; Barcelo, D. Cytostatic drugs and metabolites in municipal and hospital wastewaters in Spain: Filtration, occurrence, and environmental risk. *Sci. Total Environ.* **2014**, *497–498*, 68–77. [[CrossRef](#)]
8. Ong, W.J.; Tan, L.L.; Ng, Y.H.; Yong, S.T.; Chai, S.P. Graphitic Carbon Nitride (g-C<sub>3</sub>N<sub>4</sub>)-Based Photocatalysts for Artificial Photosynthesis and Environmental Remediation: Are We a Step Closer To Achieving Sustainability? *Chem. Rev.* **2016**, *116*, 7159–7329. [[CrossRef](#)] [[PubMed](#)]
9. Ismael, M. A review on graphitic carbon nitride (g-C<sub>3</sub>N<sub>4</sub>) based nanocomposites: Synthesis, categories, and their application in photocatalysis. *J. Alloys Compd.* **2020**, *846*, 156446. [[CrossRef](#)]
10. Nguyen, T.K.A.; Pham, T.-T.; Nguyen-Phu, H.; Shin, E.W. The effect of graphitic carbon nitride precursors on the photocatalytic dye degradation of water-dispersible graphitic carbon nitride photocatalysts. *Appl. Surf. Sci.* **2021**, *537*. [[CrossRef](#)]
11. Lima, M.J.; Silva, A.M.T.; Silva, C.G.; Faria, J.L. Graphitic carbon nitride modified by thermal, chemical and mechanical processes as metal-free photocatalyst for the selective synthesis of benzaldehyde from benzyl alcohol. *J. Catal.* **2017**, *353*, 44–53. [[CrossRef](#)]
12. Savateev, A.; Pronkin, S.; Epping, J.D.; Willinger, M.G.; Antonietti, M.; Dontsova, D. Synthesis of an electronically modified carbon nitride from a processable semiconductor, 3-amino-1,2,4-triazole oligomer, via a topotactic-like phase transition. *J. Mater. Chem. A* **2017**, *5*, 8394–8401. [[CrossRef](#)]
13. Ran, J.; Ma, T.Y.; Gao, G.; Du, X.-W.; Qiao, S.Z. Porous P-doped graphitic carbon nitride nanosheets for synergistically enhanced visible-light photocatalytic H<sub>2</sub> production. *Energy Environ. Sci.* **2015**, *8*, 3708–3717. [[CrossRef](#)]
14. Yue, B.; Li, Q.; Iwai, H.; Kako, T.; Ye, J. Hydrogen production using zinc-doped carbon nitride catalyst irradiated with visible light. *Sci. Technol. Adv. Mater.* **2016**, *12*, 034401. [[CrossRef](#)] [[PubMed](#)]
15. Tong, Z.; Yang, D.; Shi, J.; Nan, Y.; Sun, Y.; Jiang, Z. Three-Dimensional Porous Aerogel Constructed by g-C<sub>3</sub>N<sub>4</sub> and Graphene Oxide Nanosheets with Excellent Visible-Light Photocatalytic Performance. *ACS Appl. Mater. Interfaces* **2015**, *7*, 25693–25701. [[CrossRef](#)]
16. Lima, M.J.; Pastrana-Martínez, L.M.; Sampaio, M.J.; Dražić, G.; Silva, A.M.T.; Faria, J.L.; Silva, C.G. Selective Production of Benzaldehyde Using Metal-Free Reduced Graphene Oxide/Carbon Nitride Hybrid Photocatalysts. *Chem. Sel.* **2018**, *3*, 8070–8081. [[CrossRef](#)]
17. Jin, X.; Wu, Y.; Wang, Y.; Lin, Z.; Liang, D.; Zheng, X.; Wei, D.; Liu, H.; Lv, W.; Liu, G. Carbon quantum dots-modified reduced ultrathin g-C<sub>3</sub>N<sub>4</sub> with strong photoredox capacity for broad spectrum-driven PPCPs remediation in natural water matrices. *Chem. Eng. J.* **2021**, *420*, 129935. [[CrossRef](#)]
18. Morales-Torres, S.; Pastrana-Martínez, L.M.; Figueiredo, J.L.; Faria, J.L.; Silva, A.M.T. Design of graphene-based TiO<sub>2</sub> photocatalysts—a review. *Environ. Sci. Pollut. Res.* **2012**, *19*, 3676–3687. [[CrossRef](#)]
19. Ji, Y.; Cao, J.; Jiang, L.; Zhang, Y.; Yi, Z. G-C<sub>3</sub>N<sub>4</sub>/BiVO<sub>4</sub> composites with enhanced and stable visible light photocatalytic activity. *J. Alloys Compd.* **2014**, *590*, 9–14. [[CrossRef](#)]
20. Praus, P.; Svoboda, L.; Dvorský, R.; Reli, M.; Kormunda, M.; Mančík, P. Synthesis and properties of nanocomposites of WO<sub>3</sub> and exfoliated g-C<sub>3</sub>N<sub>4</sub>. *Ceram. Int.* **2017**, *43*, 13581–13591. [[CrossRef](#)]
21. Ahmed, G.; Hanif, M.; Zhao, L.; Hussain, M.; Khan, J.; Liu, Z. Defect engineering of ZnO nanoparticles by graphene oxide leading to enhanced visible light photocatalysis. *J. Mol. Catal. A Chem.* **2016**, *425*, 310–321. [[CrossRef](#)]
22. Mirikaram, N.; Perez-Molina, A.; Morales-Torres, S.; Salemi, A.; Maldonado-Hodar, F.J.; Pastrana-Martínez, L.M. Photocatalytic Performance of ZnO-Graphene Oxide Composites towards the Degradation of Vanillic Acid under Solar Radiation and Visible-LED. *Nanomaterials* **2021**, *11*, 1576. [[CrossRef](#)]
23. Li, Y.; Della Valle, F.; Simonnet, M.; Yamada, I.; Delaunay, J.-J. Competitive surface effects of oxygen and water on UV photore-sponse of ZnO nanowires. *Appl. Phys. Lett.* **2009**, *94*, 23110. [[CrossRef](#)]
24. Bizarro, M.; Sánchez-Arzate, A.; Garduno-Wilches, I.; Alonso, J.C.; Ortiz, A. Synthesis and characterization of ZnO and ZnO: Al by spray pyrolysis with high photocatalytic properties. *Catal. Today* **2011**, *166*, 129–134. [[CrossRef](#)]
25. Adekoya, D.; Qian, S.; Gu, X.; Wen, W.; Li, D.; Ma, J.; Zhang, S. DFT-Guided Design and Fabrication of Carbon-Nitride-Based Materials for Energy Storage Devices: A Review. *Nano-Micro Lett.* **2020**, *13*, 13. [[CrossRef](#)]
26. Zhu, Y.-P.; Li, M.; Liu, Y.-L.; Ren, T.-Z.; Yuan, Z.-Y. Carbon-Doped ZnO Hybridized Homogeneously with Graphitic Carbon Nitride Nanocomposites for Photocatalysis. *J. Phys. Chem. C* **2014**, *118*, 10963–10971. [[CrossRef](#)]

27. Le, S.; Jiang, T.; Li, Y.; Zhao, Q.; Li, Y.; Fang, W.; Gong, M. Highly efficient visible-light-driven mesoporous graphitic carbon nitride/ZnO nanocomposite photocatalysts. *Appl. Catal. B Environ.* **2017**, *200*, 601–610. [[CrossRef](#)]
28. de Jesus Martins, N.; Gomes, I.C.H.; da Silva, G.T.S.T.; Torres, J.A.; Avansi, W.; Ribeiro, C.; Malagutti, A.R.; Mourão, H.A.J.L. Facile preparation of ZnO:g-C<sub>3</sub>N<sub>4</sub> heterostructures and their application in amiloride photodegradation and CO<sub>2</sub> photoreduction. *J. Alloys Compd.* **2021**, *856*, 156798. [[CrossRef](#)]
29. Liu, W.; Wang, M.; Xu, C.; Chen, S. Facile synthesis of g-C<sub>3</sub>N<sub>4</sub>/ZnO composite with enhanced visible light photooxidation and photoreduction properties. *Chem. Eng. J.* **2012**, *209*, 386–393. [[CrossRef](#)]
30. Amornpitoksuk, P.; Suwanboon, S.; Sirimahachai, U.; Randorn, C.; Yaemsunthorn, K. Photocatalytic degradation of methylene blue by C<sub>3</sub>N<sub>4</sub>/ZnO: The effect of the melamine/ZnO ratios. *Bull. Mater. Sci.* **2016**, *39*, 1507–1513. [[CrossRef](#)]
31. Naseri, A.; Samadi, M.; Pourjavadi, A.; Ramakrishna, S.; Moshfegh, A.Z. Enhanced photocatalytic activity of ZnO/g-C<sub>3</sub>N<sub>4</sub> nanofibers constituting carbonaceous species under simulated sunlight for organic dye removal. *Ceram. Int.* **2021**, *47*, 26185–26196. [[CrossRef](#)]
32. Lv, H.; Ji, G.; Yang, Z.; Liu, Y.; Zhang, X.; Liu, W.; Zhang, H. Enhancement photocatalytic activity of the graphite-like C<sub>3</sub>N<sub>4</sub> coated hollow pencil-like ZnO. *J. Colloid Interface Sci.* **2015**, *450*, 381–387. [[CrossRef](#)]
33. Brunauer, S.; Emmett, P.H.; Teller, E. Adsorption of gases in multimolecular layers. *J. Am. Chem. Soc.* **1938**, *60*, 309–319. [[CrossRef](#)]
34. Sing, K.S.W.; Everett, D.H.; Haul, R.A.W.; Moscou, L.; Pierotti, R.A.; Rouquérol, J.; Siemieniewska, T. Reporting physisorption data for gas/solid systems with special reference to the determination of surface area and porosity. *Int. Union Pure Appl. Chem.* **1985**, *57*, 603–619. [[CrossRef](#)]
35. Barrett, E.P.; Joyner, L.G.; Halenda, P.P. The determination of pore volume and area distributions in porous substances. I. Computations from nitrogen isotherms. *J. Am. Chem. Soc.* **1951**, *73*, 373–380. [[CrossRef](#)]
36. Morales-Torres, S.; Pastrana-Martínez, L.M.; Figueiredo, J.L.; Faria, J.L.; Silva, A.M.T. Graphene oxide-P25 photocatalysts for degradation of diphenhydramine pharmaceutical and methyl orange dye. *Appl. Surf. Sci.* **2013**, *275*, 361–368. [[CrossRef](#)]
37. Newcombe, G.; Hayes, R.; Drikas, M. Granular activated carbon: Importance of surface properties in the adsorption of naturally occurring organics. *Colloid. Surf. A Physicochem. Eng. Asp.* **1993**, *78*, 65–71. [[CrossRef](#)]
38. Pastrana-Martínez, L.M.; Morales-Torres, S.; Papageorgiou, S.K.; Katsaros, F.K.; Romanos, G.E.; Figueiredo, J.L.; Faria, J.L.; Falaras, P.; Silva, A.M.T. Photocatalytic behaviour of nanocarbon-TiO<sub>2</sub> composites and immobilization into hollow fibres. *Appl. Catal. B Environ.* **2013**, *142–143*, 101–111. [[CrossRef](#)]
39. Orudzhev, F.F.; Aliev, Z.M.; Gasanova, F.G.; Isaev, A.B.; Shabanov, N.S. Photoelectrocatalytic oxidation of phenol on TiO<sub>2</sub> nanotubes under oxygen pressure. *Russ. J. Electrochem.* **2015**, *51*, 1108–1114. [[CrossRef](#)]
40. Pastrana-Martínez, L.M.; Morales-Torres, S.; Likodimos, V.; Figueiredo, J.L.; Faria, J.L.; Falaras, P.; Silva, A.M.T. Advanced nanostructured photocatalysts based on reduced graphene oxide-TiO<sub>2</sub> composites for degradation of diphenhydramine pharmaceutical and methyl orange dye. *Appl. Catal. B Environ.* **2012**, *123–124*, 241–256. [[CrossRef](#)]
41. Pérez-Molina, Á.; Morales-Torres, S.; Maldonado-Hódar, F.J.; Pastrana-Martínez, L.M. Functionalized graphene derivatives and TiO<sub>2</sub> for high visible light photodegradation of azo dyes. *Nanomaterials* **2020**, *10*, 1106. [[CrossRef](#)] [[PubMed](#)]
42. Li, X.; Zhang, J.; Shen, L.; Ma, Y.; Lei, W.; Cui, Q.; Zou, G. Preparation and characterization of graphitic carbon nitride through pyrolysis of melamine. *Appl. Phys. A* **2008**, *94*, 387–392. [[CrossRef](#)]
43. Xu, H.; Yan, J.; She, X.; Xu, L.; Xia, J.; Xu, Y.; Song, Y.; Huang, L.; Li, H. Graphene-analogue carbon nitride: Novel exfoliation synthesis and its application in photocatalysis and photoelectrochemical selective detection of trace amount of Cu<sup>2+</sup>. *Nanoscale* **2014**, *6*, 1406–1415. [[CrossRef](#)] [[PubMed](#)]
44. Xiang, Q.; Yu, J.; Jaroniec, M. Preparation and Enhanced Visible-Light Photocatalytic H<sub>2</sub>-Production Activity of Graphene/C<sub>3</sub>N<sub>4</sub> Composites. *J. Phys. Chem. C* **2011**, *115*, 7355–7363. [[CrossRef](#)]
45. Dong, F.; Zhao, Z.; Xiong, T.; Ni, Z.; Zhang, W.; Sun, Y.; Ho, W.K. In situ construction of g-C<sub>3</sub>N<sub>4</sub>/g-C<sub>3</sub>N<sub>4</sub> metal-free heterojunction for enhanced visible-light photocatalysis. *ACS Appl. Mater. Interfaces* **2013**, *5*, 11392–11401. [[CrossRef](#)] [[PubMed](#)]
46. Khorsand Zak, A.; Abd Majid, W.H.; Abrishami, M.E.; Yousefi, R. X-ray analysis of ZnO nanoparticles by Williamson–Hall and size–strain plot methods. *Solid State Sci.* **2011**, *13*, 251–256. [[CrossRef](#)]
47. Moreno-Castilla, C.; Maldonado-Hódar, F.J.; Carrasco-Marín, F.; Rodríguez-Castellón, E. Surface Characteristics of Titania/Carbon Composite Aerogels. *Langmuir* **2002**, *18*, 2295–2299. [[CrossRef](#)]
48. Bansal, R.C.; Donnet, J.B.; Stoeckli, F. *Active Carbon*; Marcel Dekker: New York, NY, USA, 1988.
49. Dong, F.; Li, Y.; Wang, Z.; Ho, W.-K. Enhanced visible light photocatalytic activity and oxidation ability of porous graphene-like g-C<sub>3</sub>N<sub>4</sub> nanosheets via thermal exfoliation. *Appl. Surf. Sci.* **2015**, *358*, 393–403. [[CrossRef](#)]
50. Zhong, Q.; Lan, H.; Zhang, M.; Zhu, H.; Bu, M. Preparation of heterostructure g-C<sub>3</sub>N<sub>4</sub>/ZnO nanorods for high photocatalytic activity on different pollutants (MB, RhB, Cr(VI) and eosin). *Ceram. Int.* **2020**, *46*, 12192–12199. [[CrossRef](#)]
51. Zhang, X.; Qin, J.; Hao, R.; Wang, L.; Shen, X.; Yu, R.; Limpanart, S.; Ma, M.; Liu, R. Carbon-Doped ZnO Nanostructures: Facile Synthesis and Visible Light Photocatalytic Applications. *J. Phys. Chem. C* **2015**, *119*, 20544–20554. [[CrossRef](#)]
52. Wang, J.; Wang, Z.; Huang, B.; Ma, Y.; Liu, Y.; Qin, X.; Zhang, X.; Dai, Y. Oxygen Vacancy Induced Band-Gap Narrowing and Enhanced Visible Light Photocatalytic Activity of ZnO. *ACS Appl. Mater. Interfaces* **2012**, *4*, 4024–4030. [[CrossRef](#)]
53. Al-Gaashani, R.; Radiman, S.; Daud, A.R.; Tabet, N.; Al-Douri, Y. XPS and optical studies of different morphologies of ZnO nanostructures prepared by microwave methods. *Ceram. Int.* **2013**, *39*, 2283–2292. [[CrossRef](#)]

54. Muelas-Ramos, V.; Sampaio, M.J.; Silva, C.G.; Bedia, J.; Rodriguez, J.J.; Faria, J.L.; Belver, C. Degradation of diclofenac in water under LED irradiation using combined g-C<sub>3</sub>N<sub>4</sub>/NH<sub>2</sub>-MIL-125 photocatalysts. *J. Hazard. Mater.* **2021**, *416*, 126199. [[CrossRef](#)]
55. de Sousa, J.G.M.; da Silva, T.V.C.; de Moraes, N.P.; Caetano Pinto da Silva, M.L.; da Silva Rocha, R.; Landers, R.; Rodrigues, L.A. Visible light-driven ZnO/g-C<sub>3</sub>N<sub>4</sub>/carbon xerogel ternary photocatalyst with enhanced activity for 4-chlorophenol degradation. *Mater. Chem. Phys.* **2020**, *256*, 123651. [[CrossRef](#)]
56. Wielinska, J.; Nowacki, A.; Liberek, B. 5-Fluorouracil-Complete Insight into Its Neutral and Ionised Forms. *Molecules* **2019**, *24*, 3683. [[CrossRef](#)]
57. Lin, H.H.-H.; Lin, A.Y.-C. Photocatalytic oxidation of 5-fluorouracil and cyclophosphamide via UV/TiO<sub>2</sub> in an aqueous environment. *Water Res.* **2014**, *48*, 559–568. [[CrossRef](#)]
58. Pastrana-Martínez, L.M.; Faria, J.L.; Doña-Rodríguez, J.M.; Fernández-Rodríguez, C.; Silva, A.M.T. Degradation of diphenhydramine pharmaceutical in aqueous solutions by using two highly active TiO<sub>2</sub> photocatalysts: Operating parameters and photocatalytic mechanism. *Appl. Catal. B Environ.* **2012**, *113–114*, 221–227. [[CrossRef](#)]
59. Catherine Galindo, P.J.A.K. Photodegradation of the aminoazobenzene acid orange 52 by three advanced oxidation processes: UV/H<sub>2</sub>O<sub>2</sub>, UV/TiO<sub>2</sub> and VIS/TiO<sub>2</sub>. *J. Photochem. Photobiol. A Chem.* **2000**, *130*, 35–47. [[CrossRef](#)]
60. Zheng, S.; Huang, Q.; Zhou, J.; Wang, B. A study on dye photoremoval in TiO<sub>2</sub> suspension solution. *J. Photochem. Photobiol. A Chem.* **1997**, *108*, 235–238. [[CrossRef](#)]
61. Zang, Y.; Li, L.; Li, X.; Lin, R.; Li, G. Synergistic collaboration of g-C<sub>3</sub>N<sub>4</sub>/SnO<sub>2</sub> composites for enhanced visible-light photocatalytic activity. *Chem. Eng. J.* **2014**, *246*, 277–286. [[CrossRef](#)]
62. Zhu, Z.; Yu, Y.; Dong, H.; Liu, Z.; Li, C.; Huo, P.; Yan, Y. Intercalation Effect of Attapulgite in g-C<sub>3</sub>N<sub>4</sub> Modified with Fe<sub>3</sub>O<sub>4</sub> Quantum Dots To Enhance Photocatalytic Activity for Removing 2-Mercaptobenzothiazole under Visible Light. *ACS Sustain. Chem. Eng.* **2017**, *5*, 10614–10623. [[CrossRef](#)]
63. Ma, J.; Wang, C.; He, H. Enhanced photocatalytic oxidation of NO over g-C<sub>3</sub>N<sub>4</sub>-TiO<sub>2</sub> under UV and visible light. *Appl. Catal. B Environ.* **2016**, *184*, 28–34. [[CrossRef](#)]
64. Hassani, A.; Faraji, M.; Eghbali, P. Facile fabrication of mpg-C<sub>3</sub>N<sub>4</sub>/Ag/ZnO nanowires/Zn photocatalyst plates for photodegradation of dye pollutant. *J. Photochem. Photobiol. A Chem.* **2020**, *400*, 112665. [[CrossRef](#)]
65. Yu, F.; Li, Y.; Liu, Z.; Nan, D.; Wang, B.; He, L.; Zhang, J.; Tang, X.; Liu, Y. Preparation and photocatalytic properties of ZnO nanorods/g-C<sub>3</sub>N<sub>4</sub> composite. *Appl. Phys. A* **2021**, *127*, 818. [[CrossRef](#)]